The final publication is available at

https://doi.org/10.1061/(ASCE)MT.1943-5533.0003692

Additional Information

1 **AIR-VOID SYSTEM CHARACTERIZATION OF ECO-CELLULAR CONCRETES**

2 Alba Font

3 Ph.D student, alprefon@upvnet.upv.es Universitat Politècnica de València (UPV)

4 ICITECH - Instituto de Ciencia y Tecnología del Hormigón, Grupo de Investigación en

5 Química de los Materiales (GIQUIMA), Universitat Politècnica de València, València, Spain.

6 María Victoria Borrachero

7 Ph.D, Professor, vborrachero@cst.upv.es, Universitat Politècnica de València (UPV)

8 ICITECH - Instituto de Ciencia y Tecnología del Hormigón, Grupo de Investigación en

9 Química de los Materiales (GIQUIMA), Universitat Politècnica de València, València, Spain.

10 Lourdes Soriano

11 Ph.D, lousomar@upvnet.upv.es, Universitat Politècnica de València (UPV)

12 ICITECH - Instituto de Ciencia y Tecnología del Hormigón, Grupo de Investigación en

13 Química de los Materiales (GIQUIMA), Universitat Politècnica de València, València, Spain.

14 José Monzó

15 Ph.D, Professor, jmmonzo@cst.upv.es, Universitat Politècnica de València (UPV)

16 ICITECH - Instituto de Ciencia y Tecnología del Hormigón, Grupo de Investigación en

17 Química de los Materiales (GIQUIMA), Universitat Politècnica de València, València, Spain.

18 Jordi Payá - **Corresponding author**

19 Ph.D, Professor, jjpaya@cst.upv.es; Tel.: +34 963877564

20 ICITECH - Instituto de Ciencia y Tecnología del Hormigón, Grupo de Investigación en

21 Química de los Materiales (GIQUIMA), Universitat Politècnica de València, València, Spain.

22

23

24

25

26

27

28

29

30

ABSTRACT

31

32   Cellular concrete is an alternative to conventional concrete as a low-density and high-insulating building

33   material. The eco-cellular concretes (ECC) based on the geopolymer technology have been recently

34   introduced by the scientific community. A form of ECC was herein studied, in which the fluid catalytic

35   cracking residue and the blast furnace slag were employed as precursors, the rice husk ash was utilized

36   as an alternative silica source in the activator and the aerating reagent was replaced with recycled

37   aluminum foil. Field emission scanning electron microscopy, optical microscopy and the ImageJ

38   software were employed to characterize the void distribution. Bulk density and porosity were determined

39   by hydric tests. The results revealed that lowest densities without strength loss were obtained when the

40   cementing matrix had a homogeneous void-system: similar spacing between pores, narrow size ranges

41   and non interconnected pores. A relation between open/close porosity with both density and thermal

42   conductivity was established.

43   **keywords**: cellular concrete, blast furnace slag, fluid catalytic cracking residue, rice husk ash, thermal

44   insulation, pore system.

45   **Abbreviations:**

46   TCC: Traditional cellular concrete

47   GCC: Geopolymer cellular concrete

48   ECC: Eco-cellular concrete

49   FCC: Fluid catalytic cracking residue

50   BFS: Blast furnace slag

51   RHA: Rice husk ash

52   RAF: Recycled aluminum foil

53   A: Commercial aluminum powder

54   **INTRODUCTION**

55   Traditional cellular concrete (TCC) is a Portland cement-based paste or mortar (with sand or fly ash) to

56   which a controlled aerating agent (commonly aluminium powder) is added. This hence results in a

57   lightweight high-insulation material with medium-low mechanical behavior (Ramamurthy,

58   Kunhanandan Nambiar, and Indu Siva Ranjani 2009). Compared to other construction materials, a cost-

59   effective solution, better performance and faster construction are achieved when cellular concrete is used.

60   This material is commonly employed in masonry units for floors, roofs and walls (Bremner et al. 1997).

61   Dolton and Hannah(Dolton and Hannah 2006) presented case studies of cellular concrete applications in

62   cold climates, and highlighted the easy application in an insulation solution as shallow utilities, pipeline

63   and tank, frost-protected shallow foundations or below-ground grouting voids, among others.

64   Hence density, compressive strength and thermal insulation must be assessed and controlled to obtain

65   good-performing cellular concretes. These properties are directly related with their void system

66   configuration (volume, mean diameter and distribution of formed internal air pores) (Ramamurthy,

67   Kunhanandan Nambiar, and Indu Siva Ranjani 2009). Porosity and strength are related to the empirical

68   models proposed by Narayanan and Ramamurthy(Narayanan and Ramamurthy 2000c) and by Kearsley

69   and Wainwright(Kearsley and Wainwright 2001). A concise study was done by Nambiar and

70   Ramamurthy(Nambiar and Ramamurthy 2007), which established a direct relationship between pore

71   parameters (volume, size and spacing) and the bulk density and strength of traditional cellular concretes.

72   These authors reported that pore shape did not influence final cellular concrete properties. Moreover, a

73   linear relation between thermal conductivity and dry bulk density was reported by Zhang et al. (Zhang

74   et al. 2015), and closed porosity with thermal conductivity correlations were also demonstrated by Topçu

75   et al. (Topçu and Uygunoğlu 2007). Wee et al. (Wee et al. 2006) revealed that optimal air content was

76   enclosed in the traditional cellular concretes matrix to obtain a homogeneous air-void distribution and,

77   consequently, low densities without strength loss. These authors showed that more air entrapped caused

78   mechanical behavior to worsen because of an interconnection of bigger sized pores. Othuman and Wang

79   (Othuman and Wang 2011) reported the strong influence of pore size distribution in the thermal

80   conductivity and physical properties of prediction models for cellular concrete manufacturing. Recently,

81   the same conclusion was reached by Almalkawi et al. (Almalkawi et al. 2018), who confirmed that a

82   well-organized air-bubbles system in a matrix with a more spherical shape would avoid internal water

83   circulation, which would give high compressive strength and low thermal conductivity.

84   Void system research works have mainly utilized scanning electron microscopy (SEM), mercury

85   intrusion porosimetry (MIP), gas permeability, X-ray computer tomography or optical microscopy

86   (Akthar and Evans 2010; Almalkawi et al. 2018; Nambiar and Ramamurthy 2007; Narayanan and

87   Ramamurthy 2000a; Yang et al. 2014). In recent research, the measurement of void parameters (shape,

88   size, volume and distribution) has been carried out by 2D image analysis processing and using computer

89   software, such as Avizo (Ducman and Korat 2016), Photoshop (Panesar 2013) or ImageJ (Esmaily and

90 Nuranian 2012). The bulk density and porosity of cellular concretes have been traditionally tested by

91 hydric tests (Colangelo et al. 2018; Pinilla Melo, Sepulcre Aguilar, and Hernández Olivares 2014).

92 It is well-known that the scientific community currently focuses on developing new materials that offer

93 a healthy and environmental-friendly alternative to conventional ones. TCC is 60% to 70% based on

94 Portland cement (OPC). The environmental impact of OPC and its non renewable raw materials

95 consumption have led the scientific community to investigate new alternatives.

96 The application of alkali activation or geopolymers technology to cellular concrete manufacturing has

97 rapidly gained importance in the last few years. Many authors have published works in which greener

98 geopolymer cellular concretes (GCCs) were developed and analyzed (Bai et al. 2016).

99 Fly ash and blast furnace slag (BFS) have been the most widely used precursors to new GCCs

100 development. The combination of Class F fly ash and blast furnace slag has been employed as precursors

101 by Zang et al. (Zhang et al. 2015) to develop GCC activated by sodium hydroxide (NaOH) and sodium

102 silicate dissolution. The best results were obtained for the specimen with 30% BFS and 70% fly ash,

103 which respectively yielded compressive strength, density and thermal conductivity of 3 MPa, 720 kg/m^3

104 and 0.15 W/mK (after a curing treatment consisting in: firstly 24 h at 40ºC, and then 27 days under

105 ambient conditions). More recently, Stolz et al. (Stolz, Boluk, and Bindiganavile 2018) also studied the

106 physical characteristics of GCC systems based on fly ash activated by NaOH and sodium silicate

107 solution, and by incorporating glass fibers into mixes to improve mechanical behavior. Specimens were

108 cured at room temperature, and densities between 1000 and 1400 kg/m^3 and compressive strengths from

109 3 to 9 MPa were obtained. Esmaily and Nuranian (Esmaily and Nuranian 2012) presented non autoclaved

110 GCCs by employing BFS activated with NaOH and sodium silicate. Specimens were compared

111 depending on curing temperature (70ºC, 78ºC, 87ºC). The best results were obtained for the GCCs cured

112 at 87ºC, which yielded a wet density and compressive strength of 946 kg/m^3 and 3.7 MPa, respectively.

113 The conducted experimental work included void system characterization, which determined the mean

114 diameter of samples to be 608 µm. The authors concluded that the pore structure more strongly

115 influenced compressive strength than curing treatment.

116 Xuan et al. (Xuan, Tang, and Poon 2019) introduced the use of municipal solid waste incineration bottom

117 ash (MSWIBA) combined with waste-glass powder (WGP) as a precursor. With a 20% of WGP, GCCs

118 were obtained that fell within the ranges of 494-1295 kg/m^3, 0.9-10.4 MPa and 0.14-0.38 W/mK. That

119   research work showed alternative materials with a wider internal voids size distribution than TCCs

120   (within the 0.02-3.0 mm range), but no correlation with the obtained physical characteristics was made.

121   In a recent research work, Font et al.(Font et al. 2018) presented a novel alternative cellular concrete

122   development, where the functional properties and carbon footprint were assessed. Three cellular systems

123   were studied: i) TCC based on OPC and commercial aluminum powder (A); ii) GCC by using fluid

124   catalytic cracking residue (FCC) or BFS as a precursor, activated by a traditional activating solution

125   (NaOH, plus commercial waterglass (WG), i.e., sodium silicate), and aerated by means recycled

126   aluminum foil (RAF); iii) Eco-cellular concretes, with a similar composition to GCC, where commercial

127   waterglass was replaced with rice husk ash (RHA). The physical properties of the developed cellular

128   concretes are summarized in Table 1.

129   The authors carried out a comparative carbon footprint calculation with the three cellular systems (TCC,

130   GCC and ECC) by considering the associated emissions of the components and the manufacturing

131   process. By taking the total TCC carbon footprint as a reference, the following conclusions were reached:

132   i) the use of geopolymer technology and the aluminum source replacement (GCC systems) allows to

133   reduce the total CO_2 emissions by 24% in the FCC system and by 48% in the BFS system; ii) when WG

134   was replaced with RHA, these emission was cut by 74% and 78% when using FCC and BFS,

135   respectively.

136   These results were the first evidence for an eco-friendly alternative with acceptable functional properties

137   in its applicability. At this point, a number of research steps are necessary to improve its properties and

138   to manage dose variability effects.

139   In the present work, the air-void system of the aforementioned developed materials was investigated.

140   Characterization was done by combining several techniques: i) field emission scanning electron

141   microscopy (FESEM), optical microscopy (OM), and the image software analysis were employed to

142   obtain the void size distribution; ii) bulk density and porosity were determined by hydric tests.

143   The results allowed the comparison of the internal matrix structure formed by gas expansion from the

144   aerating reaction in each material. Relations between the resulting final void-structure and the functional

145   properties of each material were established.

146   **MATERIALS AND METHODS**

147   Table 2 shows the materials employed in the present investigation and its origin. On the other hand, the

148   chemical composition of the raw materials (OPC, FCC, BFS and RHA) is summarized in Table 3.

149 A summary of the materials and the dose selected to manufacture the TCC, GCCs and ECCs in the

150 present study can be observed in the Table 4.

151 The mixing process was carried out by means of a paint mixer connected to a power drill AEG

152 SBE705RE model. The sequence to the specimen's manufacture was as follow:

153 <u>To prepare TCC</u>:

154   1.   The OPC and A were manually mixed for 2 minutes = solid phase

155   2.   The solid phase was mixed for 180 seconds with water

156 <u>To prepare GCCs and ECCs</u>:

157   1.   The precursors were co-milled with the RHA in a ball mill: i) FCC + RAF for 30 minutes,

158   obtaining the solid phase named $FCCR_m$ (D_{mean} = 18.43 µm).and ii) BFS + RAF for 20 minutes,

159   obtaining the solid phase named $BFSR_m$ (D_{mean} = 26.28 µm).

160   2.   The alkali dissolution (liquid phase) was shaken by the power drill for 30 seconds.

161   3.   The solid phase was added to the liquid phase and mixed for 180 seconds.

162 Fresh paste was put in a 4x4x4 cm^3 cubic mold (filled up to 50% of its capacity) and, because of the

163 reaction, the paste volume grew. Consequently, the final volume of the hardened aerated paste exceeded

164 0.5-1 cm over the top edge of the mold. After 24 h, this exceeding material was cut with a saw blade

165 before demolding. Then specimens were demolded and kept at room temperature until testing began.

166 The number, mean diameter and distribution of the formed internal air pores were studied by FESEM,

167 OM and the ImageJ software. A cube (4x4x4 cm^3) of each formulation was crushed in a porcelain mortar.

168 A small piece (7-10 mm) from the inner part of the cube was selected and immersed in acetone for 30

169 minutes and dried at 65ºC for 40 minutes. These samples were studied by FESEM. The FESEM

170 micrographs of the carbon-covered samples were taken by an ULTRA 55-ZEISS electron microscope

171 (at magnifications of 100x and 200x), which allows pore section configurations and pore diameters to be

172 measured. Another 4x4x4cm^3 cubic sample was cut into 2 cm-thick slices perpendicularly to the cast

173 face with a diamond rotary saw. The internal 16-cm^2 surfaces were observed under a Leica S8 APO

174 optical microscope. Pictures were taken with a Leica DFC 420 digital camera and images were processed

175 by the Leica LAS image analysis software. 8x magnifications were selected with a pixel representing 12

176 microns. Then these cut-off internal 16-cm^2 surfaces were immersed in a concentrated solution (0.4% by

177 volume) of universal dye (color vermilion 780) and universal solvent (302 NC), both from TKROM. To

178 complete pore impregnation, the submerged samples were placed inside a vessel connected to a vacuum

179 pump (Fig 1. a). An image of an impregnated surface was taken (Fig 1. b) (two images of each 16-cm^2

180 internal surface per sample). Images were digitized and processed by the ImageJ software.

181 Morphological operations (dilation, erosion, opening, closing and hole filling) to refine the shape of

182 objects, and for the conversion into the binary form, were performed. Pore diameter distribution

183 histograms were obtained by measuring all the pore diameters at the original magnification.

184 The bulk density and porosity of the cellular concretes were determined by hydric tests, which were done

185 in six cubic samples (4x4x4 cm^3) of each cellular concrete (CA, FR, FRR, SR and SRR). Specimens

186 were weighed and the natural density (ρ) was calculated after 7 curing days. Archimedes method was

187 used for bulk density (ρ_{bulk}) calculations (Equation (1) and Equation (2)) by employing still water as a

188 known density liquid (1000 kg/m^3). The cubic samples were weighed after being left to dry for 24 h in a

189 furnace at 105ºC to obtain their dry weight values (W_{dry}). Then samples were fully saturated by water

190 immersion for 24 h and weighed (saturated weight (W_{sat})). In the saturation state, specimens were

191 weighed by a hydrostatic balance (submerged weight (W_{sum})). To calculate the true density (ρ_{true})

192 (Equation (3)), a Le Chatelier flask with still water was used after crushing 20 g of each material to obtain

193 the true volume (V_{true}). The total, open and closed porosities (Φ_t, Φ_o and Φ_c) were obtained by Equations

194 (4), (5) and (6), respectively.

$$V_{bulk} = \frac{W_{sat} - W_{sum}}{\rho_{water}} \tag{1}$$

$$\rho_{bulk} = \frac{W_{dry}}{V_{bulk}} \tag{2}$$

$$\rho_{true} = \frac{W_{dry}}{V_{true}} \tag{3}$$

$$\Phi_t(\%) = \left(\frac{1 - \rho_{bulk}}{\rho_{true}}\right) \times 100 \tag{4}$$

$$\Phi_o(\%) = \left(\frac{W_{sat} - W_{dry}}{W_{sat} - W_{sum}}\right) \times 100 \tag{5}$$

$$\Phi_c (\%) = \Phi_t - \Phi_o \tag{6}$$

195 Simple linear regression and correlation between density and thermal conductivity (as dependent

196 variables) with bulk density and porosity (as explanatory variables) were carried out. The Statgraphics

197 XVII software was employed and the linear fit tool was applied. The values of the properties for each

198 alternative material (FR, FRR, SR and SRR) were considered a coefficient, obtained in relation to the

199 reference traditional cellular concrete as follows:

$$\beta_x = \frac{x_m}{x_r}$$

(7)

200 where:

201 β_x: coefficient for each property (where subscript (x) can be: ρ = natural density, k = thermal

202 conductivity, ρ_{bulk} = bulk density, ϕ_o = open porosity or ϕ_c = closed porosity) in the linear fit.

203 x_r: property value obtained for the reference material (CA)

204 x_m: property value obtained for each alternative material (FR, FRR, SR or SRR)

205 **RESULTS AND DISCUSSION**

206 The number, mean diameter and distribution of the pores obtained by FESEM, OM and the ImageJ

207 software for samples CA, FR, FRR, SR and SRR are summarized in Figures 2-6, respectively.

208 The CA sample had many pores within the 300-600 μm size range, followed by the number of pores with

209 sizes below 300 μm. A smaller proportion of pores had large diameters (from 600 to 3000 μm) and some

210 pore dimensions exceeded 3000 μm (Fig. 2). This sample presented an average pore diameter of 612 μm.

211 The pore distribution of samples FR and FRR (Fig. 3-4) were similar to many pores whose size was

212 under 300 μm and the number of pores lowered within each range for larger sizes. The FRR sample had

213 a small average number of pores/area (492 μm) compared to the FR sample (619 μm), which suggests

214 less aeration reactivity when the commercial silicate was replaced with RHA (FRR sample). As in the

215 CA sample, the FRR specimen had several pores whose size exceeded 3000 μm. For this reason, the

216 average pore diameter for FRR (649 μm) was larger than for FR (513 μm).

217 The BFS samples SR and SRR (Fig. 5-6) displayed a more homogeneous pore distribution than the other

218 cellular concretes herein studied. In these cases, many pore diameters were above 900 μm compared to

219 the CA, FR and FRR samples. Thus, the average pore diameters fell within the 804-819 μm range. The

220 SRR samples had many pores bigger than 3000 μm, with a smaller average number of pores/area and a

221 larger average diameter.

222 A trend in relation to the values of the number of pores/area and the average pore diameter exists. The

223 samples with a smaller number of pores/area (SR and SRR) yielded high average diameter values. The

224 sample with the smallest average pore diameter was FRR, which had the highest pores/area value.

225   The best cellular concrete in terms of physical (natural density) and mechanical (compressive strength)

226   properties (similarly to traditional systems) was represented by the ECC alternative system based on BFS

227   (SRR samples, 611 kg/m^3 and 4.6 MPa). By reviewing the resultant pore system distribution of SRR, the

228   air-void shape had no influence on the cellular concrete properties, which agrees with Nambiar and

229   Ramamurthy (Nambiar and Ramamurthy 2007). A wide range of pore dimensions with a homogeneous

230   distribution of pore diameters allowed us to obtain a matrix in which micropores were enclosed in the

231   walls between macropores. Thus, a lower-density material can be obtained with no major strength loss.

232   Conversely, the FR sample was the material with the highest density; as this GCC system had more

233   pores/area, the diameter range of pores was narrower than it was for the other samples.

234   Table 5 shows the bulk density and porosity (total, open and closed porosities) assessed in each studied

235   system.

236   When comparing bulk density with porosity in the alternative systems (FR, FRR, SR and SRR), a linear

237   relation was experimentally obtained. High bulk density involves a high closed porosity and,

238   consequently, a lower open porosity was obtained. This is logical if we consider that bulk density comes

239   from considering the bulk volume, which involves the solid volume and the volume entrapped in the

240   closed void of the material.

241   After comparing the materials, it can be stated that the total porosity of the CA sample was 80% and its

242   closed porosity/open porosity ratio (Φ_c/Φ_o) was 1.05, which indicates that closed porosity was similar to

243   open porosity. The FR sample had 66% total porosity with a 2.28 Φ_c/Φ_o ratio, so its relative closed

244   porosity was much higher than in the CA sample. The FRR sample obtained 70% total porosity, with its

245   Φ_c/Φ_o between the CA and FR samples (1.62). The same total porosity of FRR was obtained for SR

246   (70%), but its Φ_c/Φ_o ratio was 0.52 because the closed porosity was lower than the open porosity. Finally,

247   for the SRR sample, total porosity was 66%, which came close to the total porosity of FR but, as in the

248   SR sample, this Φ_c/Φ_o ratio was also below the unit (0.65).

249   The results of the linear fit obtained from the statistical analysis are plotted in Figure 7 for natural density

250   and in Figure 9 for thermal conductivity. These graphs reveal a positive linear dependence between

251   density and closed porosity (Fig 7.a) and a negative linear dependence between natural density and open

252   porosity (Fig 7.b). In both the resultant models, the p-value was lower than 0.05, which means that a

253   statistic significant relation between natural density and the explanatory variables (closed porosity and

254   open porosity) existed, with a 95% confidence level. The R-squared statistic allowed to affirm that

255   92.17% of natural density variability was explained by the model fit assessed with closed porosity, and

256   96.74% by the model fit assessed with open porosity. Finally, a strong dependence of natural density

257   with closed porosity and open porosity was found with a correlation coefficient of 0.96 and -0.98,

258   respectively.

259   The reduction in natural density for the systems with higher open porosity was most probably because

260   open porosity consists in the volume of pores connected to the outside boundary of the material, which

261   are filled with air. On the other extreme, the higher density of the systems when closed porosity is higher

262   than open porosity can be explained by the increasing total volume of the solid matrix: there are many

263   walls between closed pores. Furthermore, as observed in Figure 8, a direct relation appears between

264   closed porosity and the number of the smallest size pore predominance (pore size < 300 μm). Thus the

265   volume of the solid matrix in these materials was bigger and the natural density of the material increased.

266   A linear fit was found when considering all the studied systems (traditional system, CA sample, was

267   included in the fitting). The initial hypothesis of a high dependence between both variables was accepted

268   with a p-value that equaled 0.02 and the R-squared statistic equaled 92%.

269   Font et al.(Font et al. 2018) analyzed the physical properties of each alternative material (GCC and ECC

270   systems) by its relative values in relation to traditional cellular concrete ones (TCC) to obtain the natural

271   density (ϑ_d) and compressive strength (ϑ_s) ratio coefficients. The authors concluded that the relation

272   between natural density and compressive strength was direct for the FCC samples and inverse for the

273   BFS samples.

274   The models that describe the relation linking thermal conductivity with bulk density (Fig 9.a), closed

275   porosity (Fig 9.b) and open porosity (Fig 9.c) showed an intense dependence relation, which has been

276   commonly affirmed by other authors (Narayanan and Ramamurthy 2000b; Ramamurthy, Kunhanandan

277   Nambiar, and Indu Siva Ranjani 2009). The model p-value was under 0.05 for the three linear fits that

278   appeared. Thus, a statistically significant relation was found between thermal conductivity and the

279   explanatory variables (closed porosity, open porosity, bulk density), with a 95% confidence level. The

280   statistic R-square allowed to affirm that the model fit explained 97.24%, 99.55% and 97.58% of natural

281   density variation in relation to closed porosity, open porosity and bulk density, respectively. Finally, the

282   correlation coefficients were -0.98 (negative linear dependence) for closed porosity as an explanatory

283   variable, 0.99 (positive linear dependence) for open porosity as an explanatory variable and -0.98

284 (negative linear dependence) for bulk density as an explanatory variable. This means a strong dependence

285 of thermal conductivity on them.

286 **CONCLUSIONS**

287 The void-system configuration in the alternative alkali-activated cellular concretes (GCC) as well as eco-

288 cellular concretes (ECC) represents a primary influence on their functional properties (density,

289 compressive strength and thermal conductivity).

290 A relation clearly links natural densities and compressive strengths with the void-system analyzed

291 parameters (the average number of pores/area and the mean pore diameters). The development of a

292 homogeneous void distribution, with non interconnected pores, regular shapes and continuous sizes,

293 involves an alternative cellular concrete with lower natural density and enough matrix stability to achieve

294 relatively high compressive strength.

295 The amount of pores/area can be associated with aeration effectiveness, while the size of the obtained

296 pores indicates the reaction intensity. By comparing all the materials, the cellular concretes with more

297 pores/area (FR>CA>FRR>SRR>SR) achieved a more effective aerating reaction with a resulting matrix

298 in which smaller pore size ranges predominated (pores smaller than 300 μm: FR>CA ≈ FRR>SRR ≈

299 SR). The materials with fewer pores/area had bigger sized pores (pores above 3000 μm: SRR>SR>FRR

300 ≈ CA>FR), which indicates a more aggressive and less effective aerating reaction.

301 A relation between bulk density and porosity was established: with an internal void system where the

302 Φ_c/Φ_o ratio was over the unit, and bulk density was higher than when the Φ_c/Φ_o ratio was below the unit.

303 Furthermore, closed porosity resulted in a direct relation with voids distribution where smaller sizes

304 predominated. Finally, bulk density and porosity were confirmed as explanatory characteristics of the

305 thermal conductivity in the alternative cellular concretes.

306 In general, greener cellular concrete alternatives, the ECC (FRR and SRR), have an internal void system

307 with similar parameters to TCCs (CA).

308 **DATA AVAILABILITY STATEMENT**

309 Some or all data, models, or code that support the findings of this study are available from the

310 corresponding author upon reasonable request.

314 Caselles for the recycled aluminum foil, and also to the Electronic Microscopy Service of the UPV.

315 Thanks also go to DACSA, BP Oil and Cementval for supplying the raw materials.

316 **Bibliography**

317 Akthar, F. K., and J. R.G. Evans. 2010. "High Porosity (> 90%) Cementitious Foams." *Cement and*

318   *Concrete Research* 40(2): 352–58. http://dx.doi.org/10.1016/j.cemconres.2009.10.012.

319 Almalkawi, Areej T. et al. 2018. "Physio-Microstructural Properties of Aerated Cement Slurry for

320   Lightweight Structures." *Materials* 11(4): 1–15.

321 Bai, Chengying et al. 2016. "High Strength Metakaolin-Based Geopolymer Foams with Variable

322   Macroporous Structure." *Journal of the European Ceramic Society* 36(16): 4243–49.

323   http://www.sciencedirect.com/science/article/pii/S0955221916303612.

324 Bremner, Theodore W, Philip M Carkner, Michael Healy, and Albert Litvin. 1997. "Guide for Precast

325   Cellular Concrete Floor, Roof, and Wall Units." *Manual of Concrete Practice*: 2–6.

326 Colangelo, F. et al. 2018. "Mechanical and Thermal Properties of Lightweight Geopolymer Composites."

327   *Cement and Concrete Composites* 86: 266–72.

328 Dolton, B, and C Hannah. 2006. "Cellular Concrete : Engineering and Technological Advancement for

329   Construction in Cold Climates." : 1–11.

330 Ducman, V., and L. Korat. 2016. "Characterization of Geopolymer Fly-Ash Based Foams Obtained with

331   the Addition of Al Powder or H2O2 as Foaming Agents." *Materials Characterization* 113: 207–

332   13. http://dx.doi.org/10.1016/j.matchar.2016.01.019.

333 Esmaily, H., and H. Nuranian. 2012. "Non-Autoclaved High Strength Cellular Concrete from Alkali

334   Activated   Slag."   *Construction   and   Building   Materials*   26(1):   200–206.

335   http://dx.doi.org/10.1016/j.conbuildmat.2011.06.010.

336 Font, Alba et al. 2018. "New Eco-Cellular Concretes: Sustainable and Energy-Efficient Materials."

337   *Green Chemistry*.

338 Kearsley, E.P., and P.J. Wainwright. 2001. "Porosity and Permeability of Foamed Concrete." *Cement*

339   *and Concrete Research* 31(5): 805–12.

340 Nambiar, E. K Kunhanandan, and K. Ramamurthy. 2007. "Air-Void Characterisation of Foam

341   Concrete." *Cement and Concrete Research* 37(2): 221–30.

342 Narayanan, N., and K. Ramamurthy. 2000a. "Microstructural Investigations on Aerated Concrete."

343   *Cement and Concrete Research* 30(3): 457–64.

———. 2000b. "Structure and Properties of Aerated Concrete: A Review." *Cement and Concrete Composites* 22(5): 321–29.

Narayanan, N, and K Ramamurthy. 2000c. "Prediction Models Based on Gel-Pore Parameters for Compressive Strength of Aerated Concrete." 2(December): 206–12.

Othuman, Md Azree, and Y. C. Wang. 2011. "Elevated-Temperature Thermal Properties of Lightweight Foamed Concrete." *Construction and Building Materials* 25(2): 705–16. http://dx.doi.org/10.1016/j.conbuildmat.2010.07.016.

Panesar, D. K. 2013. "Cellular Concrete Properties and the Effect of Synthetic and Protein Foaming Agents." *Construction and Building Materials* 44: 575–84. http://dx.doi.org/10.1016/j.conbuildmat.2013.03.024.

Pinilla Melo, Javier, Alberto Sepulcre Aguilar, and Francisco Hernández Olivares. 2014. "Rheological Properties of Aerated Cement Pastes with Fly Ash, Metakaolin and Sepiolite Additions." *Construction and Building Materials* 65: 566–73. http://dx.doi.org/10.1016/j.conbuildmat.2013.05.082.

Ramamurthy, K., E. K. Kunhanandan Nambiar, and G. Indu Siva Ranjani. 2009. "A Classification of Studies on Properties of Foam Concrete." *Cement and Concrete Composites* 31(6): 388–96. http://dx.doi.org/10.1016/j.cemconcomp.2009.04.006.

Stolz, Jonathan, Yaman Boluk, and Vivek Bindiganavile. 2018. "Mechanical, Thermal and Acoustic Properties of Cellular Alkali Activated Fly Ash Concrete." *Cement and Concrete Composites* 94(August): 24–32. https://doi.org/10.1016/j.cemconcomp.2018.08.004.

Topçu, Ilker Bekir, and Tayfun Uygunoğlu. 2007. "Properties of Autoclaved Lightweight Aggregate Concrete." *Building and Environment* 42(12): 4108–16.

Wee, Tiong-Huan, Daneti Saradhi Babu, Tamilselvan T, and Hwee-Sin Lim. 2006. "Air-Void System of Foamed Concrete and Its Effect on Mechanical Properties." *ACI Materials Journal* 103(0889325X): 45–52. http://scholarbank.nus.edu.sg/handle/10635/84515.

Xuan, Dongxing, Pei Tang, and Chi Sun Poon. 2019. "MSWIBA-Based Cellular Alkali-Activated Concrete Incorporating Waste Glass Powder." *Cement and Concrete Composites* 95(August 2018): 128–36. https://doi.org/10.1016/j.cemconcomp.2018.10.018.

Yang, Keun Hyeok, Kyung Ho Lee, Jin Kyu Song, and Min Ho Gong. 2014. "Properties and Sustainability of Alkali-Activated Slag Foamed Concrete." *Journal of Cleaner Production* 68:

374   226–33. http://dx.doi.org/10.1016/j.jclepro.2013.12.068.

375 Zhang, Zuhua, John L. Provis, Andrew Reid, and Hao Wang. 2015. "Mechanical, Thermal Insulation,

376   Thermal Resistance and Acoustic Absorption Properties of Geopolymer Foam Concrete." *Cement*

377   *and Concrete Composites* 62: 97–105. http://dx.doi.org/10.1016/j.cemconcomp.2015.03.013.

378

Table 1. Composition and selected properties of the different cellular concretes(Font et al. 2018).

	Precursor	Aerating agent	Liquid Phase	Mixtures	Density (kg/m^3)	Compressive strength (MPa)	Thermal conductivity (W/mK)
TCC	OPC	A	Water	**CA**	618 ± 2	6.5 ± 0.4	0.182 ± 0.001
GCC	FCC		NaOH + WG	**FR**	813 ± 2	4.3 ± 0.4	0.083 ± 0.003
	BFS			**SR**	474 ± 4	2.6 ± 0.2	0.281 ± 0.007
	FCC	RAF		**FRR**	782 ± 4	3.2 ± 0.3	0.113 ± 0.005
ECC	BFS		NaOH + RHA	**SRR**	611 ± 4	4.6 ± 0.3	0.224 ± 0.007

379

Table 2. Materials and its origin

Ordinary Portland Cement (**OPC**)	Lafarge S.A
Fluid catalytic cracking residue (**FCC**)	BP Oil Company
Blast furnace slag (**BFS**)	Cementval S.A
Rice husk ash (**RHA**)	DACSA S.A
Commercial aluminum powder (**A**)	Schlenk Metallic Pigments GmbH
Recycled aluminum foil **RAF**	Department of Agricultural Forest Ecosystems at the Universitat Politècnica de València
NaOH (pellets - 98% purity)	Panreac S.A
WG (8 wt% Na_2O, 28% wt% SiO_2 and 64% wt% H_2O)	Merck-Spain

380

Table 3. Chemical compositions of OPC, FCC, BFS and RHA (wt%).

	SiO_2	Al_2O_3	Fe_2O_3	CaO	MgO	SO_3	K_2O	Na_2O	P_2O_5	TiO_2	Cl	LOI*

OPC	20.80	4.60	4.80	65.60	1.20	1.70	1.00	0.07	-	-	-	0.23
FCC	47.76	49.26	0.60	0.11	0.17	0.02	0.02	0.31	0.01	1.22	-	0.53
BFS	30.53	10.55	1.29	40.15	7.43	1.93	0.57	0.87	0.26	0.89	-	5.53
RHA	85.58	0.25	0.21	1.83	0.5	0.26	3.39	-	0.67	-	0.32	6.99

*Loss on ignition

381

Table 4. Overview of the materials and doses to the specimen's manufacture.

	Solid phase			Liquid phase				
	Precursor	Aerating agent	Dose (wt%)			w/b [2]	SiO_2/Na_2O	Na^+ molality [3]
CA	OPC [1]	A		Water		0.50	-	-
FR	FCC			Water/NaOH/WG		0.60		
FRR		RAF	2%	Water/NaOH/RHA		0.70	1.70	7.50
SR	BFS			Water/NaOH/WG		0.35		
SRR				Water/NaOH/RHA		0.45		

[1] OPC = CEM I- 52.5R

[2] w/b = water/binder ratio

[3] Na^+ molality = mol of sodium per kg of water.

382

Table 5. Values of bulk density and porosity (total, Φt; open, Φo; closed, Φc) obtained from hydric tests.

|	Bulk density (kg/m^3)	Porosity (%)		
		Φt	Φo	Φc
CA	614 ± 1	80	39	41
FR	797 ± 2	69	21	48
FRR	740 ± 2	70	27	44
SR	584 ± 2	70	46	24
SRR	616 ± 3	66	40	26

383
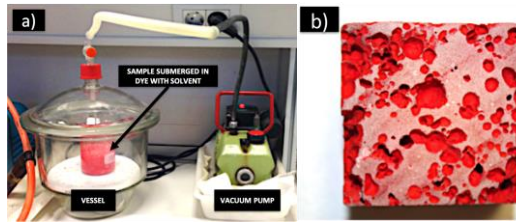
384   •

385   •   **Fig. 1.** Specimen preparation for the ImageJ analyses: a) sample immersed in color solution,

386   connected to a vacuum pump; b) the impregnated internal surface of samples (4x4 cm^2 section).
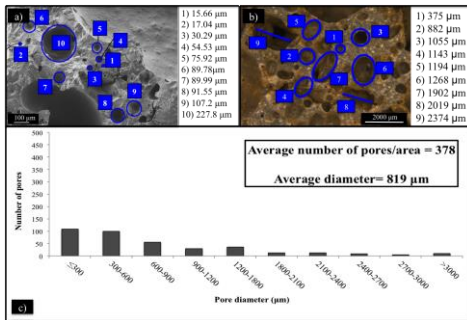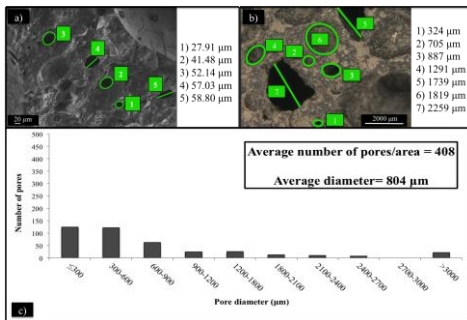
387   •
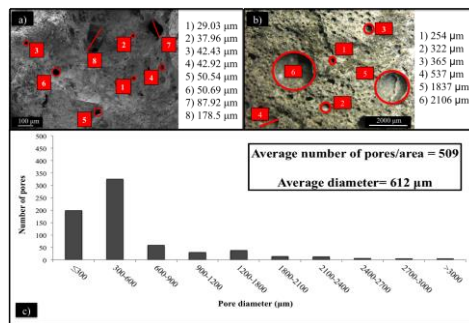
388   •

389   •   **Fig 2.** Pore system characterization of **CA**: a) FESEM micrograph at 100x magnifications with

390   pore sizing; b) OM image at 8x magnifications with pore sizing; c) pore diameter distribution

391   in the 16-cm^2 area.

392   •
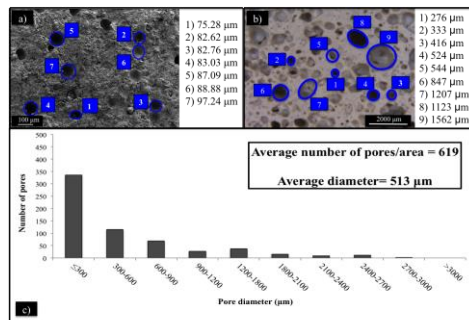
393   •

394   •   **Fig 3.** Pore system characterization of **FR**: a) FESEM micrograph in 100x magnifications with

395   pore sizing; b) OM image in 8x magnifications with pore sizing; c) pore diameter distribution

396   in the 16-cm^2 area.
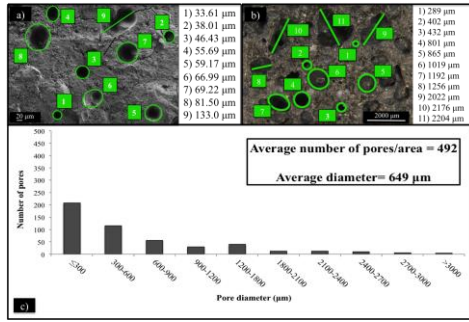
Fig 4. Pore system characterization of **FRR**: a) FESEM micrograph in 200x magnifications with pore sizing; b) OM image in 8x magnifications with pore sizing; c) pore diameter distribution in the 16-cm^2 area.


Fig 5. Pore system characterization of **SR**: a) FESEM micrograph in 100x magnifications with pore sizing; b) OM image in 8x magnifications with pore sizing; c) pore diameter distribution in the 16-cm^2 area.

Fig 6. Pore system characterization of **SRR**: a) FESEM micrograph in 200x magnifications with pore sizing; b) OM image in 8x magnifications with pore sizing; c) pore diameter distribution in the 16-cm^2 area.
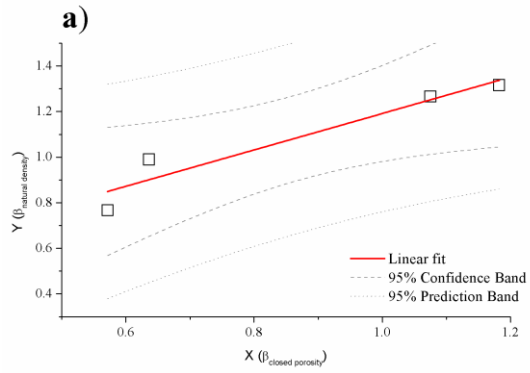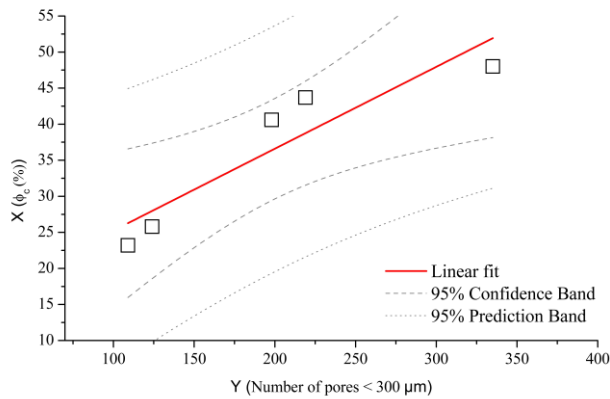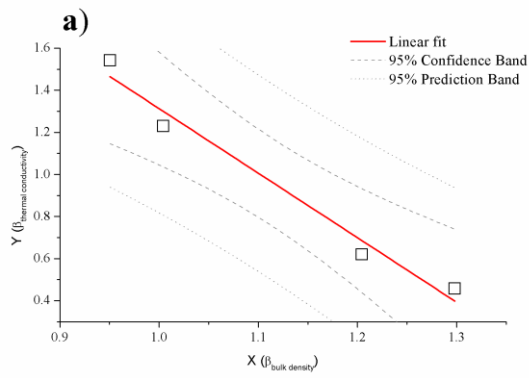
405 •
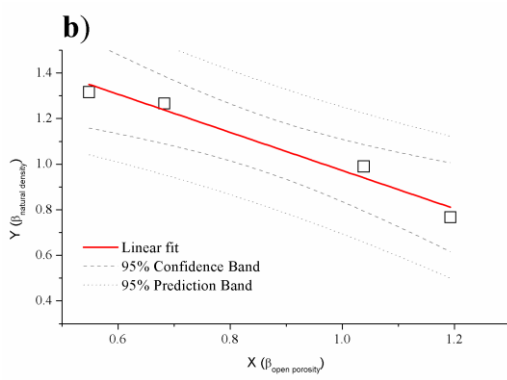
406

407 • **Fig 7.** Linear fit model for: a) natural density (dependent variable) and closed porosity

408 (explanatory variable); and b) natural density (dependent variable) and open porosity

409 (explanatory variable).

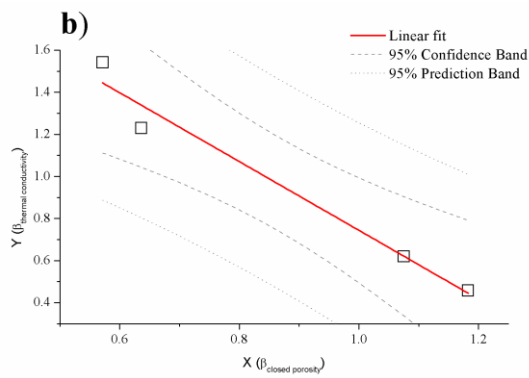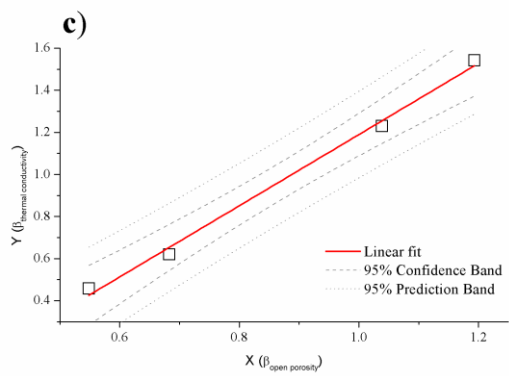

410 •

411 • **Fig 8.** Linear fit model for closed porosity (dependent variable) and number of pores smaller

412 than 300 μm (explanatory variable).

413 •

414

415

416 • **Fig 9.** Linear fit models for: a) thermal conductivity (dependent variable) and bulk density

417 (explanatory variable); b) thermal conductivity (dependent variable) and closed porosity

418 (explanatory variable); c) thermal conductivity (dependent variable) and open porosity

419 (explanatory variable)

420